RESEARCH ARTICLE

Key Points:
- Climatology of high-latitude TEC perturbations as observed by Swarm reasonably agrees with that of CHAMP published earlier
- Irregularities in the NH are aligned with the L shell, strictly in the nightside auroral/subauroral region and loosely in the polar cap
- Perturbations in the SH are poorly aligned with the L shell, possibly due to the large offset between geographic and geomagnetic poles

Correspondence to:
J. Park,
pj@kasi.re.kr

Morphology of high-latitude plasma density perturbations as deduced from the total electron content measurements onboard the Swarm constellation

Jaeheung Park[1,2] ID, Hermann Lühr[3], Guram Kervalishvili[3] ID, Jan Rauberg[3], Claudia Stolle[3,4] ID, Young-Sil Kwak[1,2] ID, and Woo Kyoung Lee[1] ID

[1]Korea Astronomy and Space Science Institute, Daejeon, Korea, [2]Department of Astronomy and Space Science, University of Science and Technology, Daejeon, Korea, [3]GFZ German Research Centre for Geosciences, Potsdam, Germany, [4]Faculty of Sciences, University of Potsdam, Potsdam, Germany

Abstract In this study, we investigate the climatology of high-latitude total electron content (TEC) variations as observed by the dual-frequency Global Navigation Satellite Systems (GNSS) receivers onboard the Swarm satellite constellation. The distribution of TEC perturbations as a function of geographic/ magnetic coordinates and seasons reasonably agrees with that of the Challenging Minisatellite Payload observations published earlier. Categorizing the high-latitude TEC perturbations according to line-of-sight directions between Swarm and GNSS satellites, we can deduce their morphology with respect to the geomagnetic field lines. In the Northern Hemisphere, the perturbation shapes are mostly aligned with the L shell surface, and this anisotropy is strongest in the nightside auroral (substorm) and subauroral regions and weakest in the central polar cap. The results are consistent with the well-known two-cell plasma convection pattern of the high-latitude ionosphere, which is approximately aligned with L shells at auroral regions and crossing different L shells for a significant part of the polar cap. In the Southern Hemisphere, the perturbation structures exhibit noticeable misalignment to the local L shells. Here the direction toward the Sun has an additional influence on the plasma structure, which we attribute to photoionization effects. The larger offset between geographic and geomagnetic poles in the south than in the north is responsible for the hemispheric difference.

1. Introduction

In recent years, most of the satellites at low Earth orbit (LEO) are equipped with dual-band receivers for Global Navigation Satellite Systems (GNSS) signals, from which we can deduce total electron content (TEC) along the line-of-sight (LOS) between the LEO and GNSS satellites [e.g., *Yue et al.*, 2011] (hereafter, "LEO-TEC"). The LEO-TEC observations have global data coverage (even above oceans), while ground-based GNSS receivers, which have been more commonly used in the community, do not. In comparison to in situ plasma density measurements (such as those by onboard Langmuir probes), the LEO-TEC measurements are benefited by simultaneous observations of multiple GNSS satellites [e.g., *Zakharenkova et al.*, 2016]. As a result, the amount of data is much larger than that of the Langmuir probe (LP) with the same cadence.

The LEO-TEC has been used in ionospheric studies such as *Heise et al.* [2002], *Mannucci et al.* [2005], *Yizengaw et al.* [2006], *Pedatella et al.* [2011], *Lee et al.* [2013], and *Lei et al.* [2015], to name a few. However, most of the studies are related rather to large-scale behavior of the ionosphere and plasmasphere than to plasma perturbations.

Usage of LEO-TEC for plasma "perturbations" has been rare, in spite of its merits. *Mitchell et al.* [2005], *Nishioka et al.* [2009], *Kinrade et al.* [2012], and *Zakharenkova and Astafyeva* [2015] investigated storm time perturbations in LEO-TEC data, but each paper focused on storm events. Based on the Constellation Observing System for Meteorology, Ionosphere, and Climate TEC data, *Pedatella and Larson* [2010] addressed the climatology of plasmapause signatures observed at the midlatitude ionosphere but did not delve into other latitude regions. *Noja et al.* [2013] presented a comprehensive statistics of high-latitude perturbations deduced from TEC measured by a single satellite, Challenging Minisatellite Payload (CHAMP). However, all the TEC data were used regardless of their LOS directions: possible differences between TEC data from different LOS directions were

not discussed in detail. Note that *Shume et al.* [2015] also addressed that the GNSS signal disturbances can be different for different GNSS satellites (i.e., for different LOS directions). Those authors used TEC observations derived from radio occultation, which are different from TEC observations derived from LEO topside antennas: the former is more sensitive to elevation and azimuth angle variations since these radio wave paths scan through larger parts of the ionized *F* region and through the *E* region.

Based on the brief review of the previous studies listed above, we can find room for further improvement in exploiting the LEO-TEC data in studying ionospheric plasma perturbations. First, simultaneous observations with multiple line-of-sights toward different GNSS satellites can give a clue as to the morphology of the LEO-TEC perturbations: for example, we may check whether the perturbations are aligned with the background magnetic field, as exemplified by the narrow field-aligned gap in *Aikio et al.* [2004, Figure 10]. So far, the merit was exploited only at low-latitude regions (|magnetic latitude (MLAT)| < 25°) by *Park et al.* [2015]. Because different physical processes are responsible for low-latitude and high-latitude plasma density perturbations (for example, generalized Rayleigh-Taylor instability for the former [e.g., *Kil*, 2015] and particle precipitation and high-speed plasma convection for the latter [e.g., *Goodwin et al.*, 2015]), we may expect new findings by applying the method of *Park et al.* [2015] to high-latitude regions. Second, no previous study on statistical distributions of LEO-TEC perturbations made use of multiple LEO satellites during the same period, which can support the robustness of the single-satellite statistics.

Therefore, this study will focus on the high-latitude LEO-TEC perturbations observed by multiple satellites. We will use TEC data from the European Space Agency's satellite constellation, Swarm, from 16 July 2014 to 15 July 2016. High-latitude plasma perturbations are known to be generated by a variety of physical processes, such as entrapment of midlatitude sunlit plasma into the polar region, particle precipitation, and localized recombination [e.g., *Hosokawa et al.*, 2016b, and references therein]. Until now, statistical studies on the high-latitude TEC perturbations have been mainly based on ground-based receivers. For example, *Prikryl et al.* [2011] demonstrated that high-latitude perturbations in ground-based TEC data are generally stronger near the cusp and nighttime auroral region than in other regions. A similar pattern can also be found in *Clausen et al.* [2016, Figure 7].

In section 2, we will describe the data sets and the processing methods. Section 3 presents a statistical distribution of TEC gradients, which will be discussed in section 4. Finally, we will summarize the main results and draw conclusions in section 5.

2. Instruments and Data Processing Methods

2.1. Satellite and Payloads
The Swarm constellation is composed of three identical satellites (Alpha, Bravo, and Charlie) launched on 22 November 2013 into a polar LEO at 500 km altitude [e.g., *Olsen et al.*, 2013; *Stolle et al.*, 2013; *Lühr et al.*, 2015]. During the first 2 months, the satellites orbited in a string-of-pearls configuration at the same altitude. Between January and April 2014, orbit maneuvers were conducted so that (1) Swarm-Alpha and Swarm-Charlie fly side by side at altitudes around 470 km (2) and Swarm-Bravo flies about 50 km higher than the lower pair. Due to a slightly different precession rate, the local time (LT) of Swarm-Bravo's orbital plane gradually departs from those of the lower pair. Each of the Swarm spacecraft carries a Precision Orbit Determination (POD) antenna, from which TEC between Swarm and GNSS satellites can be estimated. The sampling cadence of the GNSS data from the POD antenna was originally 10 s, but the data rate of all three satellites was changed to 1 Hz in July 2014. In this study, we use the Swarm Level 2 (L2) TEC data, with the product identifier of SW_OPER_TECxTMS, where "x" is the satellite identifier (A, B, or C). Detailed descriptions on the TEC product are given at the following Web page: https://earth.esa.int/documents/10174/1514862/ Swarm_Level-2_TEC_Product_Description. The analysis period is from 16 July 2014, when the 1 Hz sampling of POD data was fully established, to 15 July 2016. In this study, we mainly focus on Swarm-Alpha and Swarm-Bravo because they are at two different orbit altitudes.

We complement the TEC data with in situ plasma density measured by the onboard LPs. The Level 1b LP data have the product identifier of SW_OPER_EFIx_PL_1B or SW_PREL_EFIx_LP_1B. All the Swarm data are available at the official data distribution site at https://earth.esa.int/web/guest/swarm/data-access.

Merits of Swarm/TEC in comparison with CHAMP/TEC [e.g., *Noja et al.*, 2013] are as follows. First, the TEC sampling rate of the former satellite is 10 times higher than that of the latter. Second, multiple LEO satellites at different altitudes exist for the Swarm project, while the CHAMP was a stand-alone satellite mission.

2.2. Data Processing Methods

The original Swarm/TEC data are slant TEC (STEC) along the LOS from Swarm to GNSS satellites. However, STEC generally gets larger as the corresponding GNSS satellite moves from the zenith to the horizon due to the longer ray pass through the ionosphere. When comparing TEC values (or gradients) from different LOS directions, which is one of the prime purposes of this paper, the statistics is expected to be biased toward larger STEC values (or gradients) for near-horizon LOS directions. Hence, we mitigate the bias by calculating equivalent vertical TEC (hereafter, "VTEC" or "LEO-VTEC") as has been done frequently by previous papers [e.g., *Mannucci et al.*, 2005]. This procedure can be considered as normalization of LEO-VTEC by alleviating its dependence on the distance the GNSS signal travels through the ionosphere.

We use the obliquity function of *Garcia-Fernàndez and Montenbruck* [2006, equation (15)], which originates from *Lear* [1987]:

$$\text{VTEC} = \text{STEC} \times \frac{\sqrt{\sin^2 \theta + 0.076} + \sin \theta}{2.037} \tag{1}$$

where θ is the elevation angle toward a GNSS satellite: it is 90° when the GNSS satellite is at the zenith of Swarm. The minimum elevation angle of the Swarm TEC data product is 20°. Note that the resultant VTEC value (e.g., at time t_0) is assigned to the position of Swarm at the epoch (t_0) of the GNSS observation.

In this study, we define |ΔTEC| at a given time t_0 and for a given GNSS satellite as follows:

$$|\Delta\text{TEC}|(t_0) = \frac{|\text{VTEC}(t_0 - 1s) - \text{VTEC}(t_0)| + |\text{VTEC}(t_0 + 1s) - \text{VTEC}(t_0)|}{2} \tag{2}$$

where $\text{VTEC}(t_0)$ is the LEO-VTEC at time t_0. By using the absolute values of the VTEC differences, we can guarantee that |ΔTEC| is a nonnegative measure of the VTEC perturbation level. If a |ΔTEC| value is unreasonably large (>100 total electron content unit, 1 TECU $= 10^{16}$ el m^{-2} (TECU)), the data point is discarded. Also, the |ΔTEC| is not calculated over a time gap longer than or equal to 2 s: therefore, three seamlessly consecutive data points are needed to calculate a |ΔTEC| value. Note that the horizontal scale size corresponding to equation (2) is about 7.5 km/s × 2 s ≈ 15 km. It is generally larger than the Fresnel size that can cause GNSS scintillations (subkilometer-scale sizes) [e.g., *Muella et al.*, 2010]. Hence, the term "perturbation" instead of "irregularity" is used for denoting |ΔTEC| throughout this paper because the latter is often used for denoting scintillation-producing inhomogeneities of plasma density.

Our analyses are not significantly affected by differential code bias in TEC data because we are only interested in the |ΔTEC|, which is free from the daily differential code bias. Note that our method may be compromised by cycle slips and resultant unphysical TEC jumps. However, standard methods of cycle slip detection and correction [e.g., *Noja*, 2010; *Noja et al.*, 2013] are used in generating the Swarm/TEC data. Furthermore, cycle slips are frequently accompanied with time gaps (temporary loss of lock [e.g., *Xiong et al.*, 2016]), which are filtered out by our data analysis method. Hence, we expect that the effects of unphysical cycle slips have been minimized. We may note that an error in slant-to-vertical TEC conversion increases for low-elevation angles and keep this fact in mind when interpreting the results in the following sections.

Considering the time needed for Swarm to cover all LT sectors (~131 days), the three seasons are defined in the following way. June and December seasons span 131 days around 21 June and 21 December, respectively. Combined equinox is defined as 65 days around 21 March and 21 September.

|ΔTEC| values are bin averaged in various ways, such as in geographic latitude (GLAT)-by-geographic longitude (GLON) space, in magnetic latitude (MLAT)-by-magnetic local time (MLT) space, and in LOS direction space, which will be detailed in the following subsection. The MLAT and MLT are based on the quasi-dipole coordinate system [*Richmond*, 1995]. As the current paper focuses on high-latitude plasma perturbations, only TEC data points at |MLAT| ≥ 55° are considered in the data processing.

2.3. LOS Direction Space

Figure 1 presents two examples of Swarm/TEC data, which pictorially demonstrate the prime motivation of this study. The first rows of Figures 1a and 1b present plasma density measured by the onboard LP. In the second rows, VTEC curves are shown in different colors for different GNSS satellites identified by their
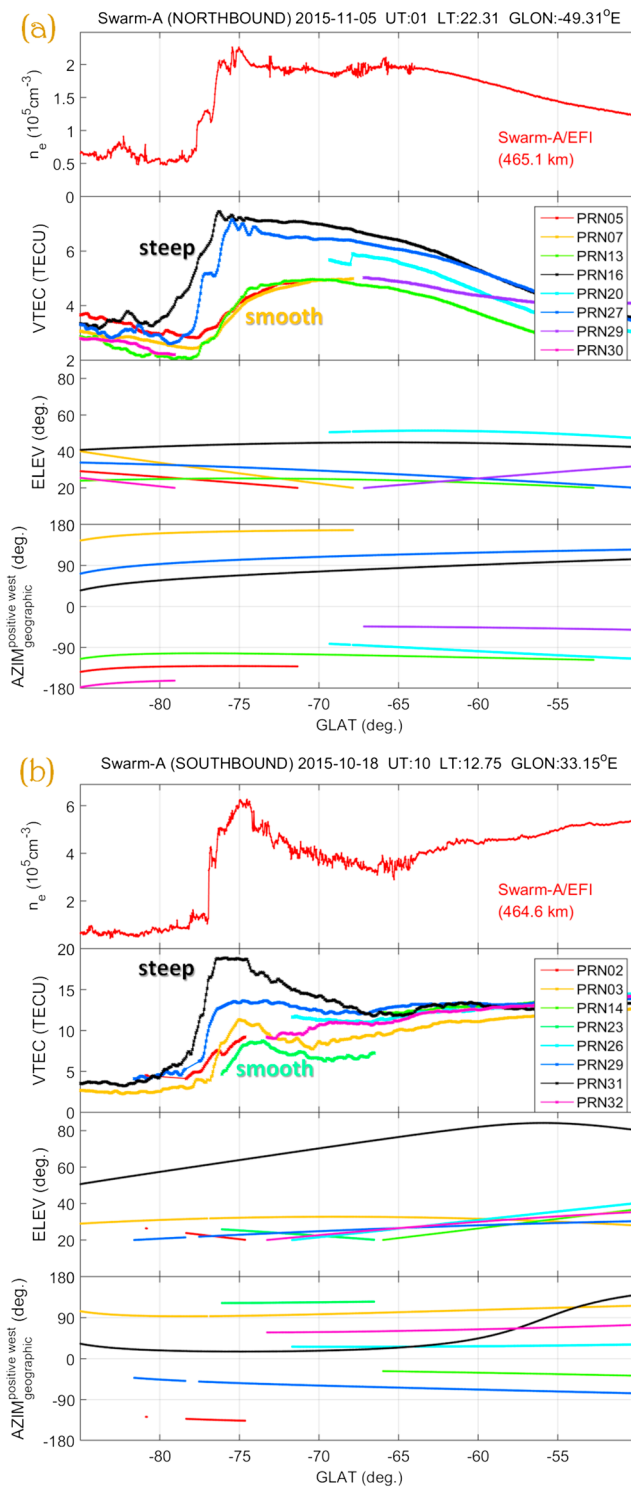
Figure 1. Two examples of Swarm/TEC data: (first rows) plasma density measured by the onboard LP, (second rows) VTEC with different colors for different GNSS satellites, and (third and last rows) elevation and azimuth angles toward each GNSS satellite.

pseudorandom noise (PRN) numbers. The third and last rows show the elevation and azimuth angle of each GNSS satellite, respectively. The azimuth angle is defined as the deviation from geographic north in a counterclockwise (i.e., from north to west) direction.

In the figure, we see that different GNSS satellites report different magnitudes of LEO-VTEC gradients although all of them generally follow the trend of in situ plasma density measured by the Swarm/LP. For example, in Figure 1a, PRN 16 (black) and PRN 27 (deep blue) report steeper LEO-VTEC gradients than the other GNSS satellites do. Similarly, LEO-VTEC gradients in Figure 1b also exhibit significant difference for different GNSS satellites. The different LEO-VTEC gradients for different PRNs cannot be explained solely by their elevation angles. For example, PRN 27 (deep blue) and PRN 07 (orange) in Figure 1a had similar elevation angles at $-80°$ $\sim -75°$GLAT, but their LEO-VTEC gradients exhibit notable differences. Similarly, PRN 29 (deep blue) and PRN 02 (pure red) in Figure 1b had similar elevation angles at $-80°$ to $-75°$GLAT, but their LEO-VTEC gradients are also quite different. As TEC values corresponding to different GNSS satellites have different LOS directions (a combination of elevation and azimuth angles), the LOS directions seem to be the key factor which determines the magnitude of the LEO-VTEC gradient. In other words, the GNSS-dependent LEO-VTEC gradient in Figure 1 seems to result from the anisotropy of ionospheric perturbations: they should have some preferred directions. The open question is, what is the most favorable LOS direction (e.g., field-aligned direction) to observe the steepest LEO-VTEC gradient? It is one of the prime motivations of this study.

Figure 2a illustrates the coordinate system used for LOS directions. We use the mean field-aligned (MFA) coordinate system, where the z axis is along the mean geomagnetic field, the y axis perpendicular to the magnetic meridian (positive eastward), and the x axis completes the triad pointing toward higher L shells. For the mean geomagnetic field, we use the International Geomagnetic Reference Field (IGRF) routine available at http://kr.mathworks.com/matlabcentral/fileexchange/34388-international-geomagnetic-reference-field-igrf-model/content/igrf.m. Note that the IGRF model is used instead of the real B field data from Swarm in order to speed up the data processing. Anyhow, we expect only minor changes if we use the Swarm B field data for the mean geomagnetic field. A unit LOS vector from Swarm to a GNSS satellite is decomposed into its three components, of which the sum of squares should result in unity. Figure 2b is a three-dimensional perspective of Figure 2a.

Figure 3 schematically illustrates how $|\Delta TEC|$ can be displayed in the "LOS direction space." We use a cylindrical system where the abscissa (horizontal axis) and ordinate (vertical axis) represent the y and z axes in MFA coordinates and the amount of x is related with the length of the pointer ρ $(= \sqrt{y^2 + z^2})$. That is to say, $|x| = \sqrt{1 - \rho^2}$. The $+1$ value on the abscissa in the LOS direction space (y component in the MFA coordinate system) represents that the LOS from Swarm to a GNSS satellite is purely horizontal and toward the magnetic east: hence, the elevation angle of the GNSS satellite should be identically zero. The $+1$ and -1 values on the ordinate in the LOS direction space (z component in the MFA coordinate system) represent that the LOS from Swarm to a GNSS satellite is parallel and antiparallel to the mean geomagnetic field, respectively. The origin of this space ($\rho = 0$) corresponds to an LOS exactly normal to the local L shell: either inward or outward. The LOS directions tangent to the local L shell should trace the circumference of the unit circle in the LOS direction space ($\rho = 1$). Note that (1) the GNSS satellites are always at higher altitudes than Swarm and (2) we are mainly interested in high-latitude regions where B field lines are nearly vertical (either upward or downward). When Swarm is in the Northern Hemisphere (NH), the LOS toward GNSS satellites should always have a negative ("antiparallel") MFA z component (because the mean geomagnetic field is heading toward the ground where no GNSS satellite exists). When Swarm is in the Southern Hemisphere (SH), the LOS toward GNSS satellites should have a positive ("parallel") MFA z component. Hence, the data points in the lower half of the circle in Figure 3 (i.e., when the MFA z component is negative) come from observations in the NH, while those above the abscissa are from the SH.

Most GNSS satellites cannot reach high-latitude regions because of the limited orbit inclination angles (55°). As high-latitude B field lines are approximately radial, one may worry that no truly field aligned LOS can be observed in the high-latitude region. We have calculated the occurrence rate of nearly field aligned LOS (field aligned within 25°, which corresponds to $z \geq 0.9$) at every geographic location of Swarm/TEC data. Except for a portion of the polar cap ($|MLAT| > 80°$), in all the other magnetic latitudes of interest ($|MLAT| \geq 55°$), nearly field aligned LOS are observed, at least occasionally: see supporting information for details. This fact supports the validity of our statistical analysis in the LOS direction space.
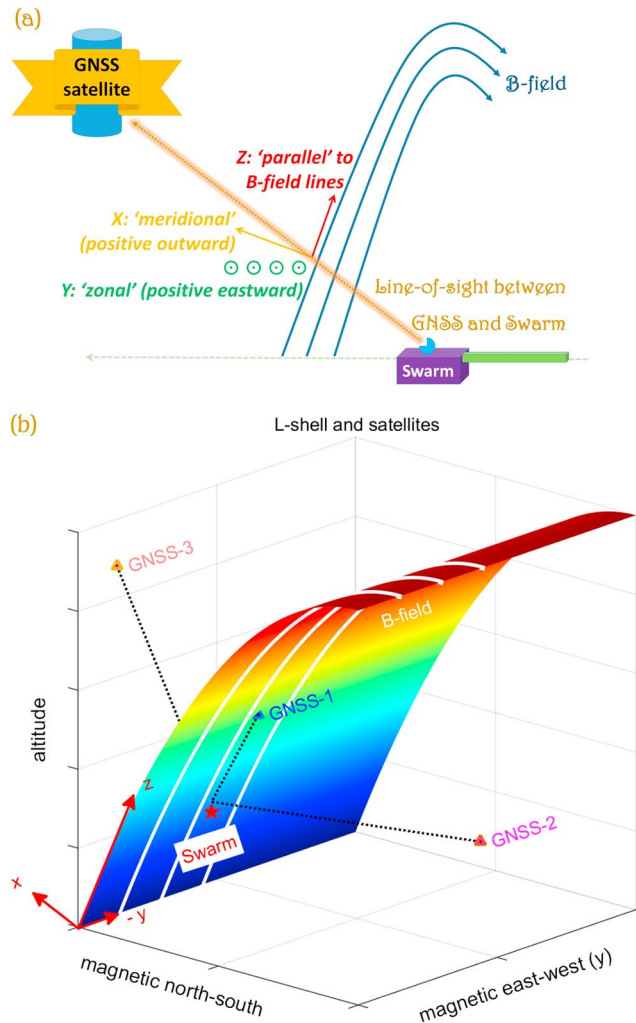
Figure 2. (a) Illustration of the coordinate system used for LOS directions: the mean field-aligned coordinate system. (b) Three-dimensional perspective of Figure 2a.
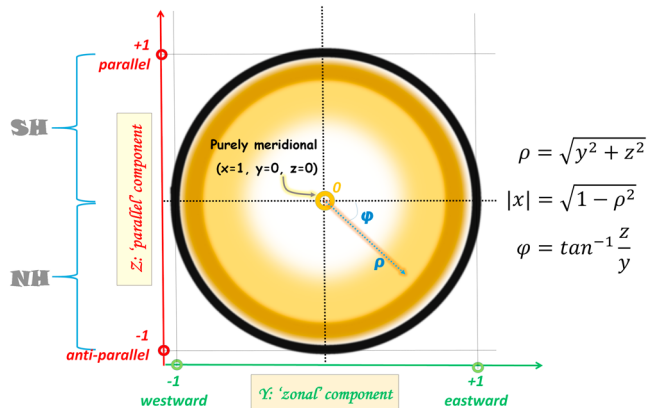
Figure 3. Illustration of the "LOS direction space." The +1 and −1 values on the ordinate (vertical axis) represent that the LOS from Swarm to a GNSS satellite is parallel (the Southern Hemisphere) and antiparallel (the Northern Hemisphere) to the mean geomagnetic field, respectively. The +1 value on the abscissa (horizontal axis) represents that the LOS from Swarm to a GNSS satellite is purely horizontal and toward the magnetic east.

One of the main purposes of this study is to deduce perturbation morphology from the |ΔTEC| distribution in the LOS direction space. In order to reach the aim, we need to focus on Swarm/TEC observations when the satellite is traversing in situ plasma density perturbations [e.g., *Park et al.*, 2015]. Otherwise, the distribution of |ΔTEC| in the LOS direction space may not faithfully reflect the "morphology" of in situ perturbations but may be affected by the (possibly random) "location" of remote perturbations. As LEO-TEC perturbations are closely correlated with in situ plasma density variations [*Zakharenkova et al.*, 2016], the effect of remote perturbations on |ΔTEC| seems small. Nevertheless, we introduce the safety measures described below to confirm that Swarm satellites are traversing in situ perturbations. For detecting the in situ plasma density perturbations, we conduct the following procedures with the Swarm/LP data (data rate = 2 Hz). First, we apply a low-pass median filter (window size = 3 LP data points ≈ 11 km) to avoid outliers in in situ plasma density. Second, we remove large-scale trends obtained by a Savitzky-Golay filter (order = 2, window size = 31 LP data points ≈116 km). The maximum amplitude of the residuals ($|\delta n_e|^{max}$) is recorded within a 15 s period (≈1° GLAT). For every |ΔTEC| data point, we check whether the corresponding 15 s interval has a $|\delta n_e|^{max}$ value above a certain threshold. Only when the in situ threshold is exceeded is the |ΔTEC| accepted in the LOS direction space. Otherwise, the |ΔTEC| is set to zero. The threshold for the $|\delta n_e|^{max}$ is empirically set to be 5×10^3 cm^{-3} for Swarm-Alpha and half of that for Swarm-Bravo, considering its higher altitude.

3. Statistical Results

3.1. Climatology in the MLAT-MLT Space

Figures 4 and 5 show bin-averaged |ΔTEC| in terms of the MLAT-MLT coordinates of Swarm-Alpha (Figure 4) and Swarm-Bravo (Figure 5). Note that the thresholding by Swarm/LP data residuals is not applied to these figures, in order that we can see the general trend in |ΔTEC| distribution. Each panel corresponds to a Lloyd season (combined equinox/June/December) and hemisphere (NH/SH). Concentric circles are given every 10° in MLAT, and the center of the circles represents the magnetic pole. The unit of |ΔTEC| is 1×10^{-3} TECU = 1×10^{13} m^{-2}. The MLT noon and midnight are toward the top and bottom of each panel, respectively (see the middle row). The regions shown in Figures 4 and 5 are divided into square-shaped bins whose sides have a length of 2° in MLAT (about 220 km by 220 km) in both magnetic noon-midnight and dawn-dusk directions. All the |ΔTEC| values in a given bin are accumulated and then divided by the number of data points, which results in bin averages of |ΔTEC|. Notable features in the figures can be summarized as follows:

1. Dayside cusp (around MLT noon, |MLAT| = 70°–80°) and nighttime auroral region (around MLT midnight, |MLAT| = 60°–70°) exhibit larger |ΔTEC| values than in the other regions.
2. High-latitude |ΔTEC| is generally larger in the Southern Hemisphere (SH) than in the Northern Hemisphere (NH). This trend can be found for all months except for June solstice.
3. High-latitude |ΔTEC| in June is smaller than that in the other seasons.

The above-mentioned points are consistent with [*Noja et al.*, 2013, Figure 4].

The morphological similarities between Swarm-Alpha (Figure 4) and Swarm-Bravo (Figure 5) data are striking, especially if we consider the different precession rates and orbital periods of the spacecraft. That is to say, Swarm-Bravo generally does not fly right above Swarm-Alpha, but their relative positions are continuously changing due to the different orbits [see *Zakharenkova et al.*, 2016, Figure 1, for example]. Hence, we cannot check whether the two satellites encounter the same plasma structures at the two heights. Nevertheless, the statistical results in Figures 4 and 5 are consistent with each other. As for quantitative comparisons, we note that |ΔTEC| is generally larger for Swarm-Alpha (at the lower altitude) than for Swarm-Bravo (at the higher altitude), which is as expected from the reduced LOS length for Swarm-Bravo in comparison with that for Swarm-Alpha. If we only consider regions with significant |ΔTEC| (i.e., |ΔTEC| ≥ 10×10^{-3} TECU) in Figures 4 and 5, the median |ΔTEC| ratio of Swarm-Bravo to Swarm-Alpha per hemisphere per season is 82–97%. It represents <20% decrease of |ΔTEC| over 50 km in altitudes.

3.2. Climatology in the GLAT-GLON Space

Figures 6 and 7 show bin-averaged |ΔTEC| in geographic coordinates for Swarm-Alpha (Figure 6) and Swarm-Bravo (Figure 7). Each panel corresponds to a season (equinox/June/December) and hemisphere (NH/SH). Coastlines are overplotted on the |ΔTEC| color maps. The white areas around the geographic poles reflect the fact that the orbit inclination angles of Swarm are slightly less than 90°. Note that the SH map is as seen from the North Pole toward the south through a transparent Earth. The regions shown in Figures 6 and 7 are again divided into square-shaped bins whose sides have a length of 2° in GLAT. Also here, the thresholding
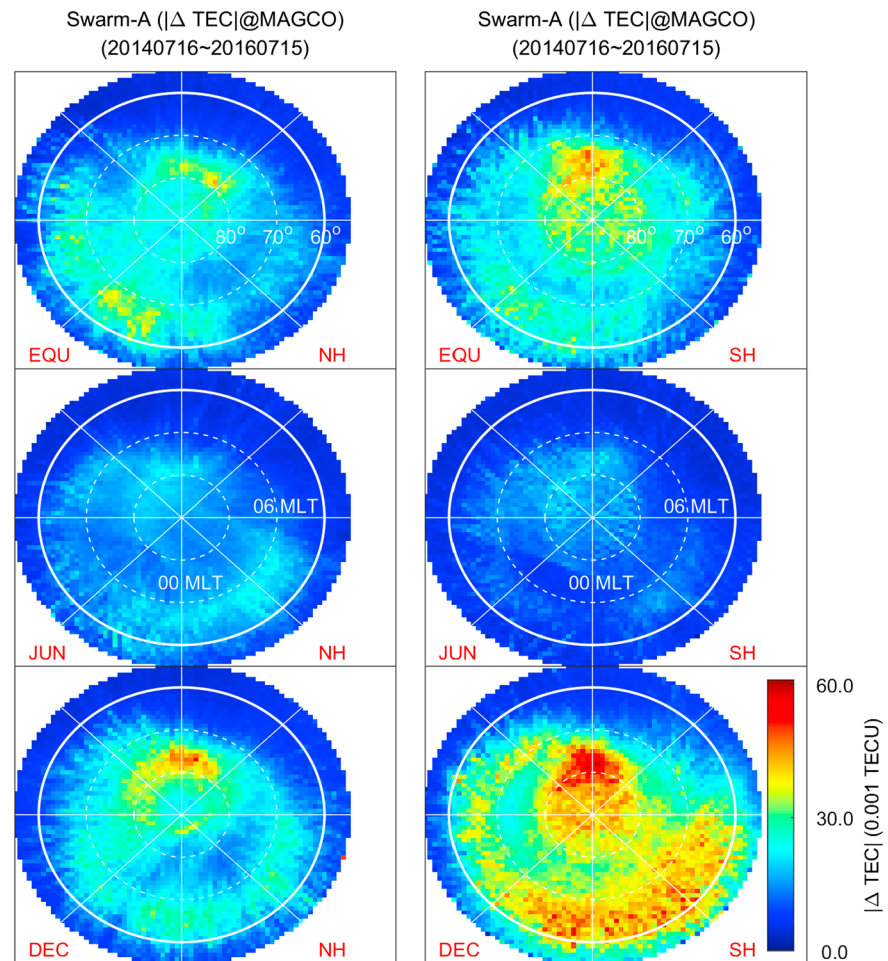
Figure 4. Bin-averaged |ΔTEC| in the MLAT-MLT coordinates for Swarm-Alpha. Each row corresponds to a season (equinox/June/December), while the left and right columns represent the Northern and Southern Hemispheres, respectively.

by Swarm/LP data residuals, as mentioned in section 2, is not applied to these figures, because the method is intended for the LOS direction space. Notable features in Figures 6 and 7 are as follows:

1. In the NH, |ΔTEC| is larger around the west coast of Greenland and Arctic Northern Canada than in the other regions.
2. In the SH, |ΔTEC| is larger around Wilkes Land and Victoria Land (heading toward Australia) than in the other regions.

These characteristics are also in general agreement with those of *Noja et al.* [2013, Figure 4]. The consistency among the CHAMP [*Noja et al.*, 2013], Swarm-Alpha, and Swarm-Bravo data supports the reliability of our data analysis method. It is interesting to note that Figures 6 and 7 appear similar to the maps of reduced-dynamic carrier-phase residuals shown in *IJssel et al.* [2016, Figure 9].

Furthermore, the Swarm results are in morphological agreement with ground-based GNSS observations [e.g., *Prikryl et al.*, 2011, Figure 6] as well as with in situ (not TEC) observations onboard CHAMP [e.g., *Park et al.*, 2012] in that the perturbations are strong at the cusp and around the nightside substorm region. *Park et al.* [2012] noticed earlier that the only difference between the ground-based and LEO GNSS observations is the seasonal variations of the perturbation occurrence: semiannual for ground-based observations (with maxima at equinoxes) and annual for those from LEO (with peak near December solstice). It was attributed to possible contribution of *E*-layer disturbances which are located between the LEO satellite and ground: hence,
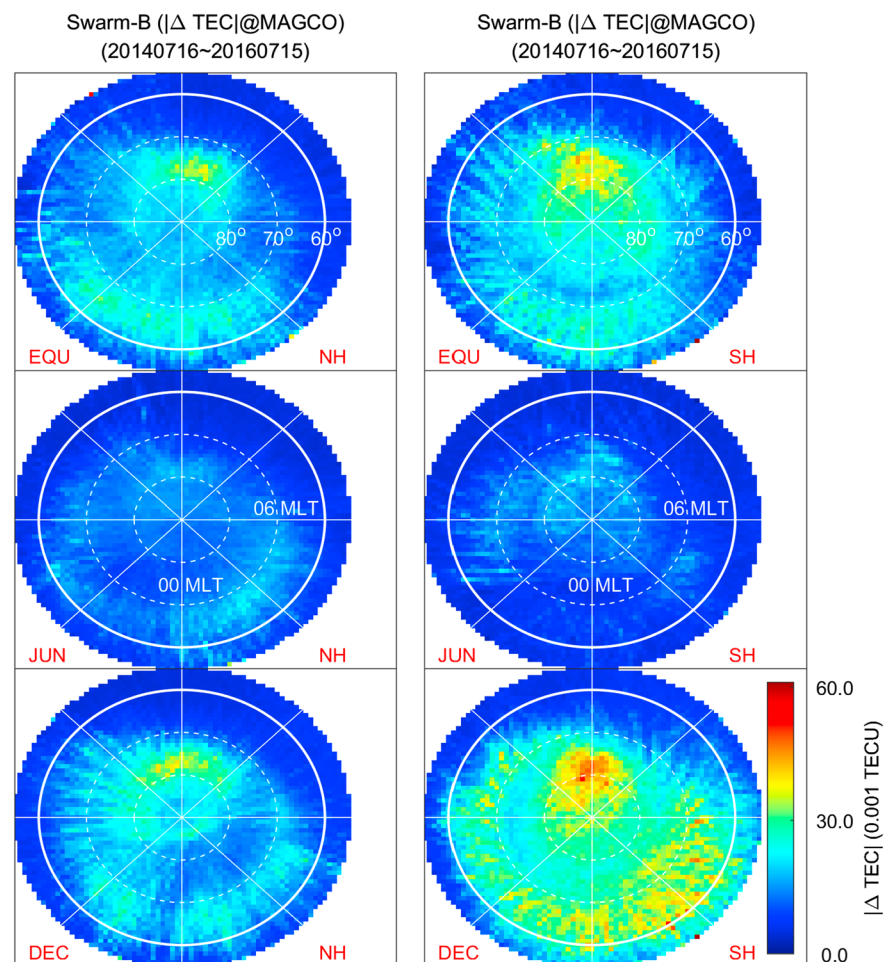
Figure 5. The same as Figure 4, but for Swarm-Bravo.

only signals received at the ground are affected by the *E*-layer disturbances. Our Swarm results exhibit annual variations with the maximum during December solstice (see Figures 4 and 5), which agrees with earlier in situ observations of the CHAMP satellite [*Park et al.*, 2012].

3.3. Climatology in the LOS Direction Space

The |ΔTEC| climatology in the LOS direction space is constructed in this subsection, but separately for the four subregions, as described in Figure 8. The categorization of the subregions is based on the |ΔTEC| climatology in geomagnetic coordinates, as shown in Figure 4. First, the "cusp" region is defined as the region within $70° \leq$ |MLAT| $\leq 80°$ and $0900 \leq$ MLT ≤ 1500 (see Figure 8). The "substorm" ("subauroral") region represents the region bounded by the following conditions: $60° \leq$ |MLAT| $\leq 70°$ ($50° <$ |MLAT| $< 60°$) and within ±5 h in MLT around midnight. The "polar cap" region is defined by the following MLAT condition: |MLAT| $> 80°$.

In Figures 9 and 10, results are presented in panels corresponding to the subregions (cusp, substorm, polar cap, and subauroral regions). Figure 9 is obtained from Swarm-Alpha data and Figure 10 from Swarm-Bravo data. In each panel, the bin-averaged |ΔTEC| is presented in the LOS direction space, which is defined by the MFA $x/y/z$ components as shown in Figure 3. If a GNSS satellite is, for example, on the horizon and toward magnetic east from Swarm, the corresponding |ΔTEC| is assigned to $(x, y, z) = (0, 1, 0)$ in the MFA coordinate system; this point will be placed on the abscissa in Figures 9 and 10. If a LOS from Swarm to a GNSS satellite is parallel to the mean geomagnetic field, the corresponding |ΔTEC| is assigned to $(x, y, z) = (0, 0, 1)$ in the MFA coordinate system; this point will be placed on the ordinate in Figures 9 and 10. If a LOS from Swarm to a
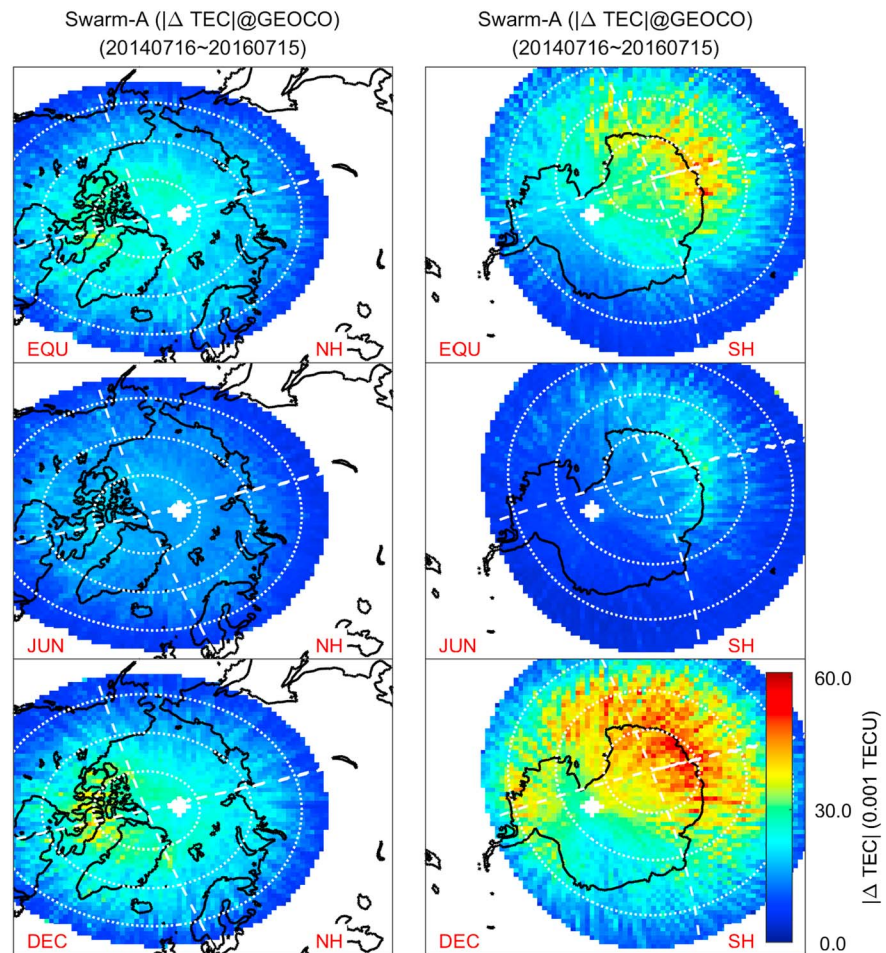
Figure 6. Bin-averaged |ΔTEC| in the geographic coordinate system for Swarm-Alpha. The white dotted ovals represent MLAT = 60°, 70°, and 80°. The white dashed lines correspond to four values of magnetic longitude: 0°, 90°, 180°, and 270°.

GNSS satellite is normal to the local L shell, the corresponding |ΔTEC| is assigned to $(x, y, z) = (\pm1, 0, 0)$ in the MFA coordinate system; this point will be placed at the center of the unit circle in Figures 9 and 10. Note that a logarithmic scale is used for the color bar for the sake of visibility. Underpopulated (bin population <200 data points) bins are kept blank. The black asterisks and triangles, which are added to guide the readers' eyes, represent deviation from the field-aligned direction by 45° along the zonal and meridional directions, respectively. The unit circle with the radius of 1 ($\rho = 1$) is also shown in each panel.

The LOS-MFA space is binned with squares of 0.05 by 0.05. Data gaps in the LOS-MFA space (shown as white areas in Figures 9 and 10) are mainly due to the lowest limit of the GNSS elevation angle in the Swarm/L2 TEC product (= 20°). For example, no Swarm/TEC data exist for purely zonal LOS (i.e., ±1 along the abscissa in Figures 9 and 10) because the corresponding elevation angle is zero. Similarly, no Swarm/TEC data are available for purely meridional LOS in the polar cap region (i.e., around the origin in Figures 9 and 10) because the corresponding elevation angles are also very small. In the subauroral region, the geomagnetic dip angle is lowest among all the considered subregions. As a result, the purely meridional LOS (normal to the L shell) is not strictly horizontal (i.e., the corresponding GNSS elevation angles are not strictly zero) in this subregion. This is why bins around the origin are well populated in Figures 9d and 10d.

In Figures 9 and 10, the NH results (i.e., the areas below the abscissa) show circular symmetry in the y–z plane of the MFA coordinate system. On the contrary, the SH results (i.e., the areas above the abscissa) exhibit notable deviations from the circular symmetry. Therefore, we start with the discussion on the NH results while
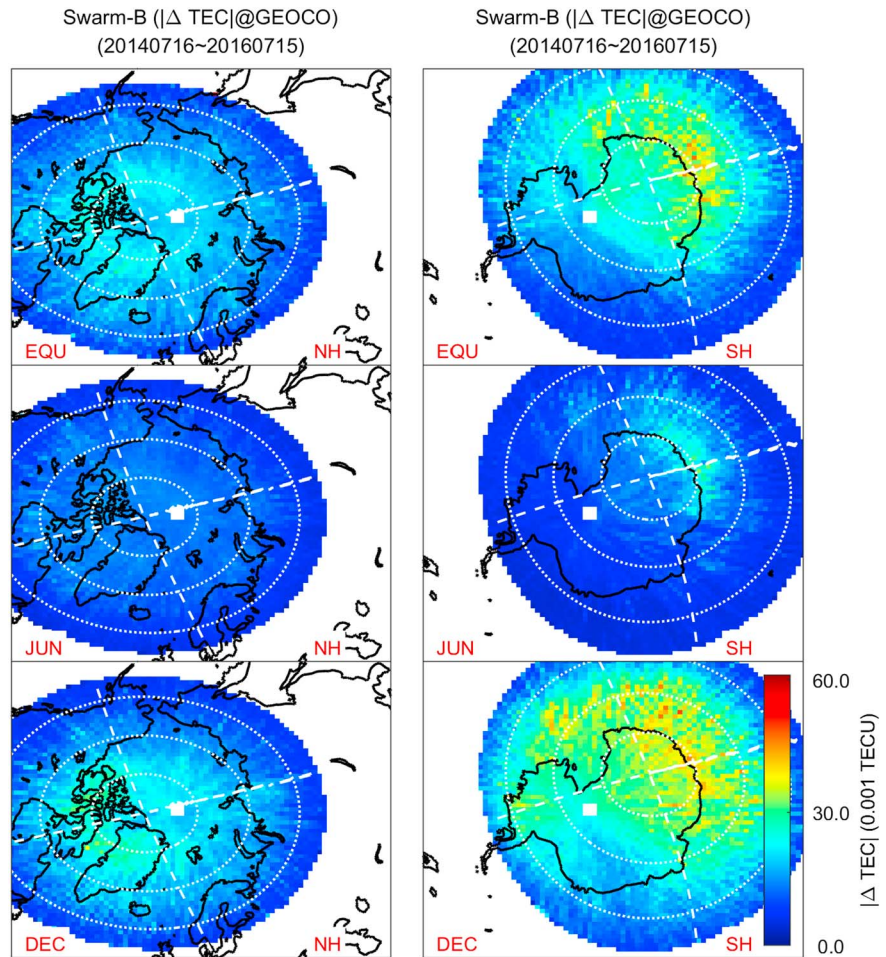
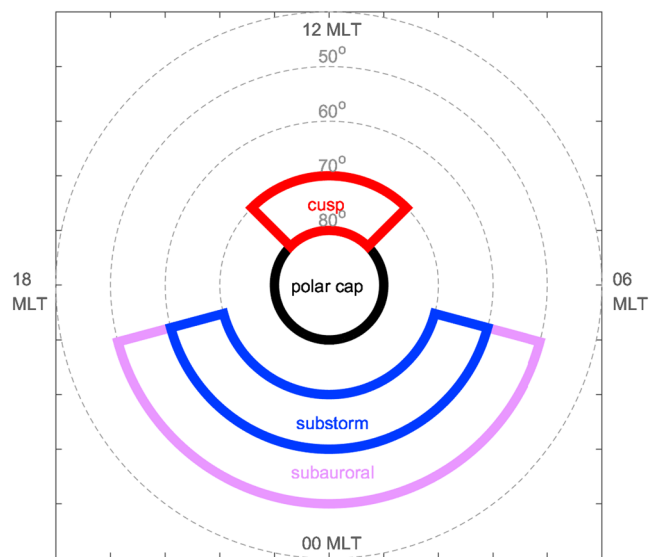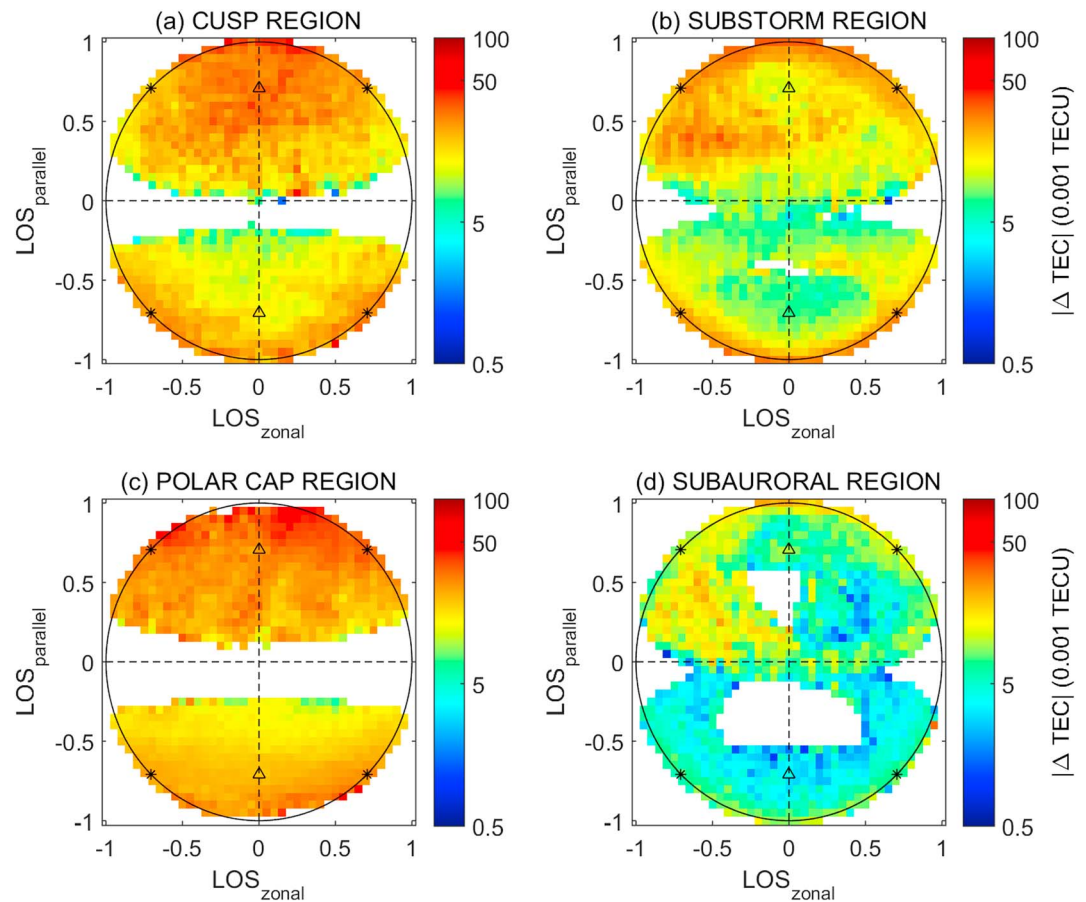**Figure 7.** The same as Figure 6, but for Swarm-Bravo.

Figure 8. The categorization of the subregions on the basis of the |ΔTEC| climatology in geomagnetic coordinate system.

Figure 9. Bin-averaged |ΔTEC| of Swarm-Alpha presented in the LOS direction space. Each panel corresponds to a subregion (cusp, substorm, polar cap, and subauroral regions). Underpopulated (bin population <200 data points) bins are shown as white.

discussions on the SH results will be deferred to the next section. The |ΔTEC| in the NH exhibits the following characteristics:

1. The |ΔTEC| at the subauroral region is generally smaller than that at the other subregions.
2. In each subregion, high |ΔTEC| values are concentrated around the circumference of the unit circle (i.e., $\rho = 1$ in Figure 3). Equivalently, an LOS need not be strictly field aligned ($z = \pm1$ in Figure 3) to get strong |ΔTEC| as long as the LOS is tangent to the local L shell ($\rho = \sqrt{y^2 + z^2} = 1$ in Figure 3).
3. As ρ becomes smaller (i.e., as the LOS deviates from the plane tangent to the local L shell), |ΔTEC| generally decreases. This trend is most conspicuous around the ordinate of Figures 9 and 10 (i.e., $z = \pm1$ in Figure 3).
4. If we compare the |ΔTEC| at the black triangles with those at the asterisks, |ΔTEC| is higher at the latter. It means that, when an LOS deviates by 45° from the direction parallel to the B field, the corresponding |ΔTEC| is expected to be larger when the deviation is toward the magnetic east/west than when it is toward a direction normal to the local L shell.
5. The |ΔTEC| in the polar cap (substorm and subauroral) region decreases most gradually (steeply) as ρ becomes smaller.

4. Discussion

4.1. Morphology of the High-Latitude LEO-VTEC Perturbations in the NH

Figure 11 schematically illustrates how the dependence of |ΔTEC| on LOS directions, as shown in Figures 9 and 10, can be used to deduce the morphology of the high-latitude ionospheric perturbations. Because of the thresholding by in situ plasma density fluctuations ($|\delta n_e|^{max}$; see section 2.3), the results in Figures 9 and 10 should reflect the configurations where Swarm itself is engulfed in perturbations. Cartoons in Figure 11 are based on this expectation. Figures 11a and 11b represent two situations where LOS directions are
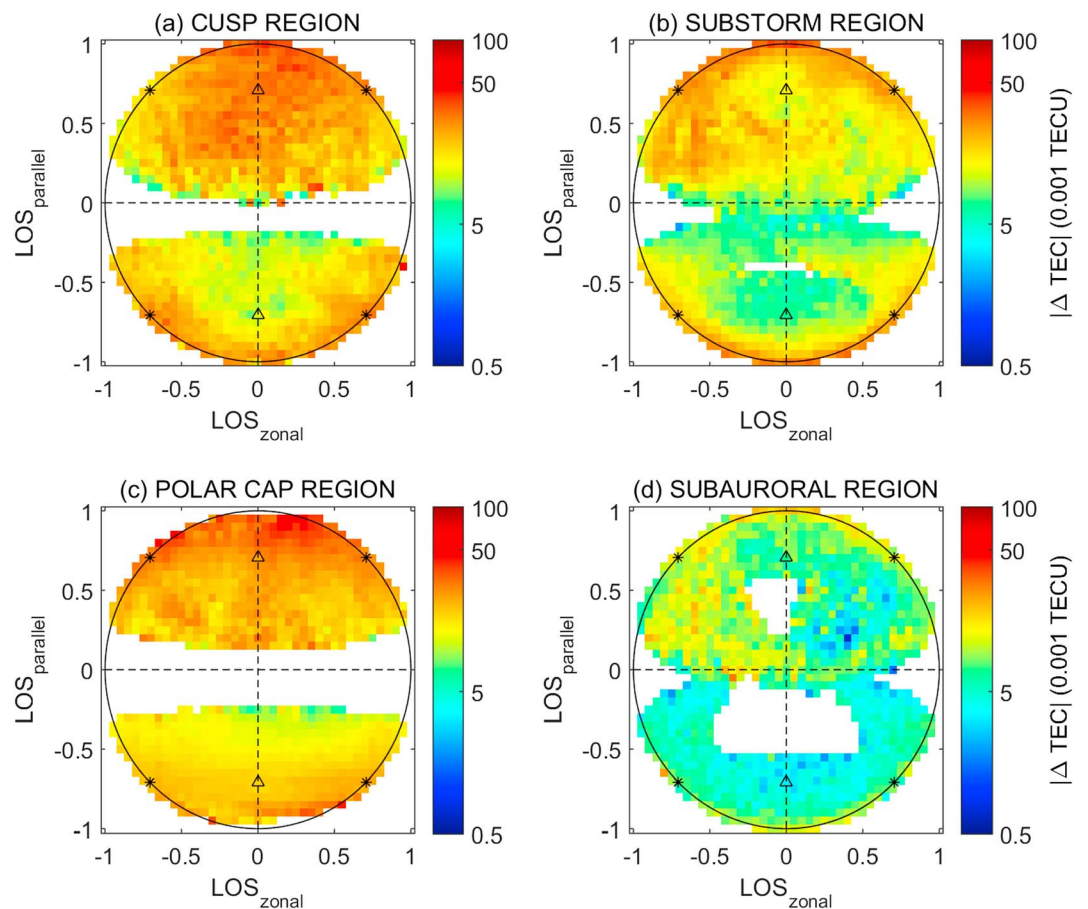
Figure 10. The same as Figure 9, but for Swarm-Bravo.

tangent and perpendicular to the ionospheric perturbation surface, respectively. In both cases, the perturbation is assumed to be well aligned with the background magnetic field (i.e., exhibiting strong anisotropy). In Figure 11a, Swarm will see a steep LEO-VTEC gradient (or high |ΔTEC|) while it moves with an orbital speed of about 7.5 km/s through the perturbation. In Figure 11b, Swarm cannot see a steep LEO-VTEC gradient along its orbit because of the field-aligned shape of the perturbation; a part of the perturbation is intersected by the LOS between Swarm and the GNSS satellite for a considerable fraction of the orbit pass. Hence, the LOS directions related to high |ΔTEC| in Figures 9 and 10 can be interpreted as directions along which high-latitude ionospheric perturbations are elongated (i.e., the preferred direction of elongation). Figures 11c and 11d illustrate observations where the perturbation has weak anisotropy with respect to the background magnetic field: i.e., we cannot tell whether the perturbation is aligned with the *B* field or not. In those cases, no big difference is expected among |ΔTEC| values for different LOS directions. With the help of Figure 11, the Swarm observational results in the NH in Figures 9 and 10 can be interpreted as follows:

1. The high-latitude LEO-VTEC perturbations are preferentially tangent to the local L shell (i.e., the two-dimensional surface defined by the two MFA coordinate axes, "parallel *z*" and "zonal *y*").
2. The anisotropy of the perturbations (i.e., their tangential alignment with the local L shell) is strongest in the substorm and subauroral regions (like in Figures 11a and 11b) and weakest inside the polar cap (like in Figures 11c and 11d). The degree of anisotropy in the cusp region is in-between.

Item 1 agrees with a case study of *Forte et al.* [2016, Conclusions] in that *F* region plasma density perturbations have two-dimensional surface structures. Note also that "ground-based" GNSS receivers at auroral latitudes may also observe enhanced phase scintillations when the LOS is aligned with the L shell: but the effect is not conspicuous [*Forte and Radicella*, 2004].
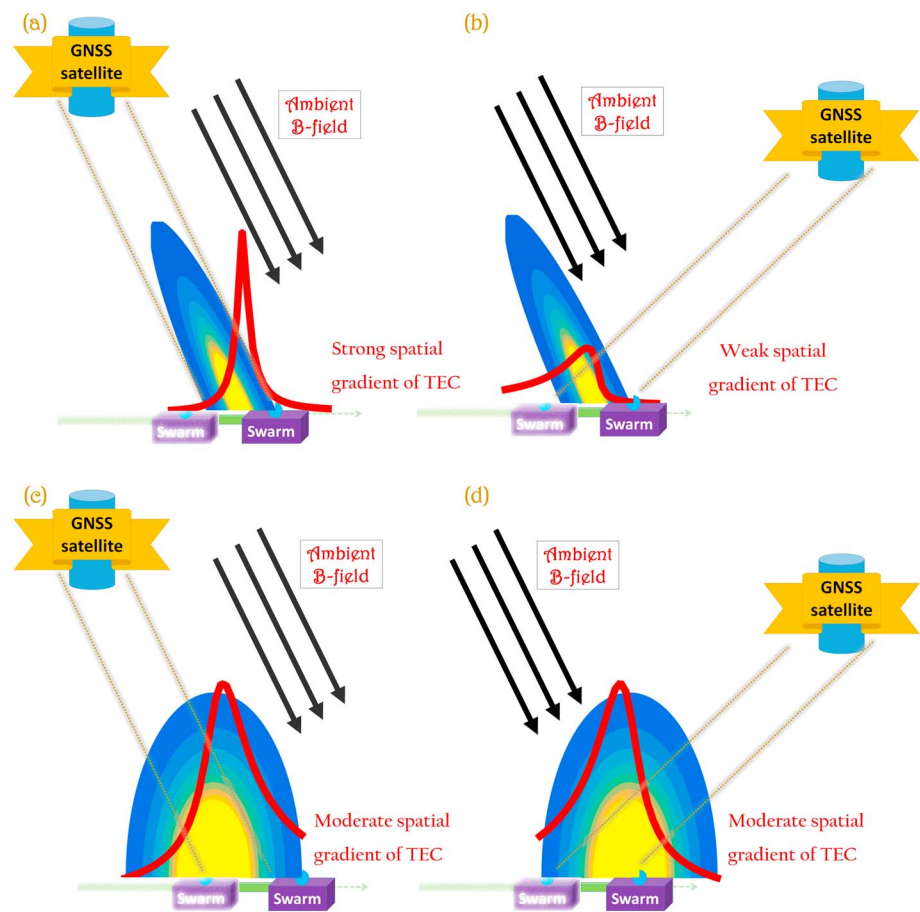
Figure 11. (a, b) Illustration of two situations where ionospheric perturbations are well aligned with the background magnetic field: LOS directions are tangent (Figure 11a) and perpendicular (Figure 11b) to the ionospheric perturbation surface. (c, d) Two situations where ionospheric perturbations exhibit weak anisotropy with respect to the background magnetic field: LOS directions are nearly tangent (Figure 11c) and near-perpendicular (Figure 11d) to the ionospheric perturbation surface.

4.2. Insolation Effects on the SH |ΔTEC| Climatology in the LOS Direction Space

In this section, we address the origin of the complex behavior of |ΔTEC| in the SH, as shown in Figures 9 and 10; the SH perturbations are not well aligned with the plane tangent to the local L shell. The offset between the geographic and geomagnetic poles is more significant in the SH than in the NH. In the SH, therefore, the morphology of insolation effects (expected to be ordered by geographic coordinates) on high-latitude |ΔTEC| (e.g., different photoionization rates in the sunlit and dark areas) may interfere significantly with that of the magnetospheric/ionospheric electrodynamics. The latter (magnetospheric/ionospheric electrodynamics) is expected to be well aligned with the MFA coordinate because (1) B field lines are usually considered as equipotentials and (2) the potential difference (or E field) should be the main driver of topside plasma dynamics. On the contrary, the former (insolation effect) should result in poor alignment with the MFA coordinates.

Figure 12 is similar to Figure 9, but the horizontal axis represents the sunward component of the LOS unit vector: +1 for sunward LOS (solar zenith angle 0°), 0 for solar zenith angle 90°, and −1 for antisunward LOS (solar zenith angle 180°). Our calculation of the solar zenith angle (SZA) is based on the information at https://en.wikipedia.org/wiki/Solar_zenith_angle. The right (left) half of each panel represents the sunlit (dark) hemisphere. The top (bottom) half of each panel is for the SH (NH), as in Figure 9. Note also that only the |ΔTEC| data points accompanied by significant in situ plasma density fluctuations ($|\delta n_e|^{max}$; see section 2.3) are taken into account, as was done for Figure 9. By the way, it has to be noted that the direction to the Sun is not necessarily at a right angle to the B field lines (see illustrations in Figure 14). Therefore, we observe |ΔTEC| values outside the circles in Figures 12 and 13 (see cusp and polar cap regions on dayside). The cusp region, which is located on the MLT dayside, has limited data coverage for $LOS_{sunward} < 0$. For example, an LOS in
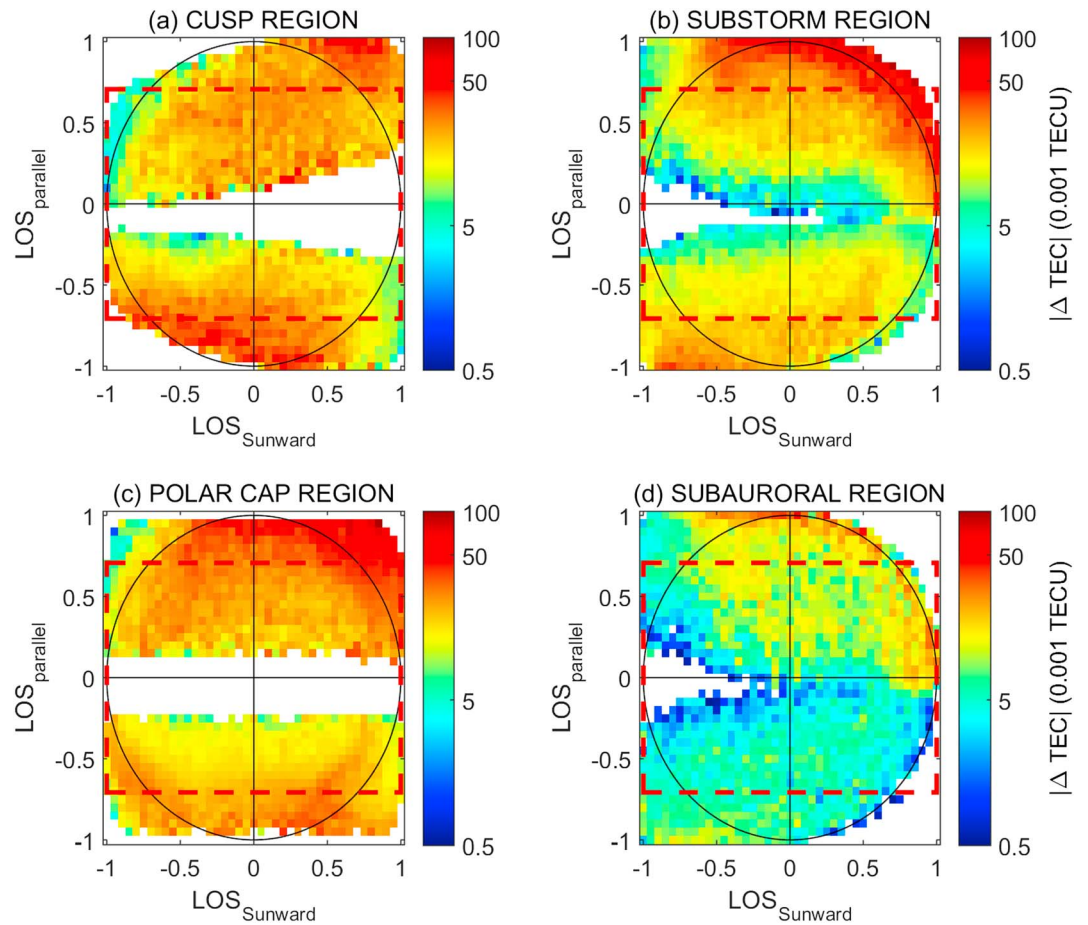
Figure 12. Similar to Figure 9, but with the horizontal axis representing the LOS component toward the Sun (+1: perfectly sunward LOS; −1: perfectly antisunward LOS).

the cusp cannot be simultaneously antisunward ($LOS_{sunward} \sim -1$) and field aligned ($|LOS_{parallel}| \sim 1$). In a similar context, the substorm and subauroral regions, which are on the MLT nightside, have limited data coverage for $LOS_{sunward} > 0$. An LOS in the substorm and subauroral regions cannot be simultaneously sunward ($LOS_{sunward} \sim +1$) and field aligned ($|LOS_{parallel}| \sim 1$).

In Figure 12, the |ΔTEC| in the SH (the upper half of each panel) is larger in the sunlit hemisphere (the right half of each panel) than in the dark hemisphere (the left half of each panel). The opposite is generally true for the NH (the lower half of each panel). These results are consistent with *Noja et al.* [2013, Figure 2] in that the SH (NH) perturbations prefer the local summer (winter) conditions, where the high-latitude region is mostly sunlit (dark). In other words, both the NH and SH perturbations preferentially occur during the December solstice. *Noja et al.* [2013, p. 300] attributed this annual cycle to the similar annual variations of the global ionospheric density.

In Figure 12, the level of |ΔTEC| for non-field-aligned LOS (e.g., $|LOS_{parallel}| < \cos(45°) \approx 0.7$; see the region inside the red dashed rectangle in each panel) generally appears higher in the SH than in the NH. This feature agrees, as expected, with that shown in Figure 9. Focusing on the non-field-aligned LOS in the SH, we further find that large |ΔTEC| values are concentrated at angles close to Sun-aligned (right border of the frame) direction (see the cartoon in Figure 14), in particular for polar cap and substorm regions. An instructive example of Sun-induced density gradient can be seen in the substorm region of the SH. In the top right frame of Figure 9b, we find enhanced |ΔTEC| values in the westward half for $LOS_{parallel} = 0.3 - 0.5$ (i.e., for westward LOS). The large |ΔTEC| values for the considered $LOS_{parallel}$ range appear at closely Sun-aligned directions. This implies that the relevant LOS directions point toward the Sun from Swarm located around the sunset terminator. This situation can occur in the premidnight sector during local summer. Figure 13 from Swarm-Bravo data exhibits
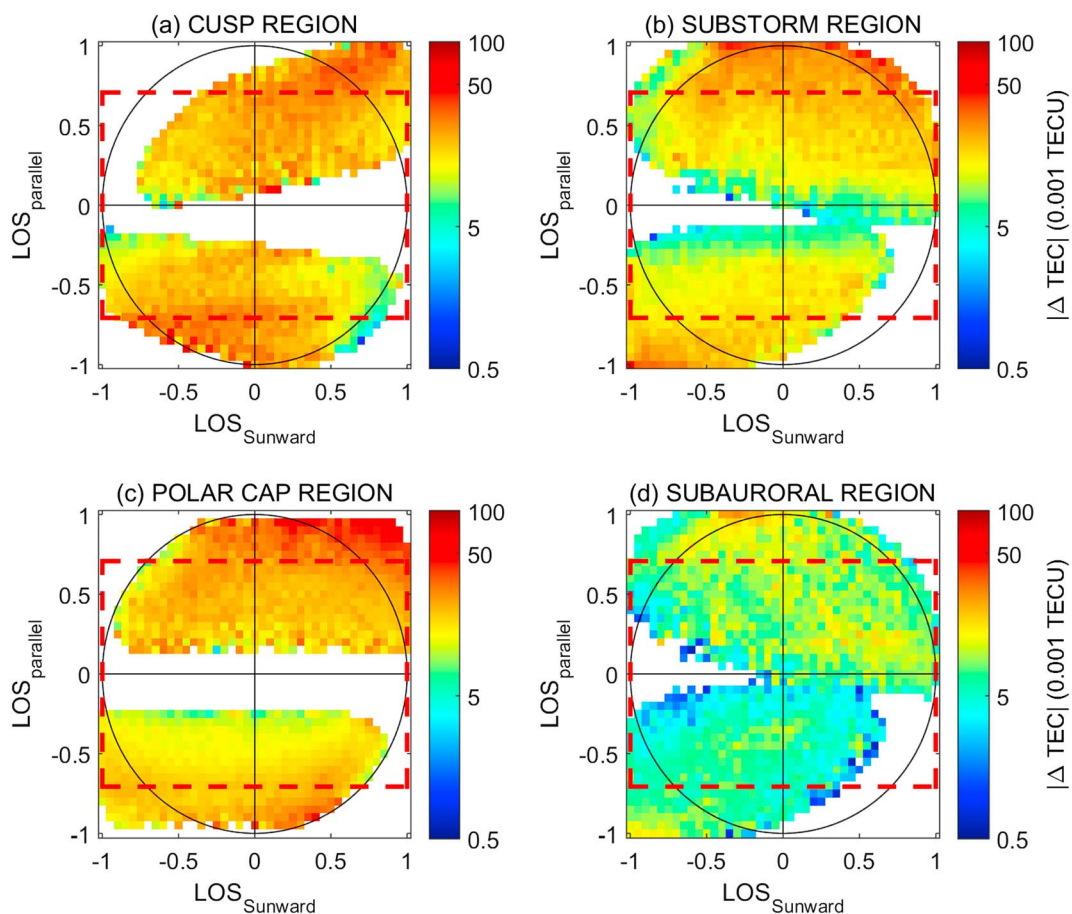
Figure 13. The same as Figure 12, but for Swarm-Bravo.

qualitatively similar SZA dependences to that of Figure 12. In summary, $|\Delta TEC|$ in the SH can be large even when $LOS_{parallel}$ is small and $LOS_{sunward}$ is large, which implies significant effects of insolation (see Figure 14).

To give further support to our inferences, we reprocess the data to create Figures 15 and 16, which are the same as Figures 9 and 10, but based solely on data points from local winter hemispheres (NH: during the December season, and SH: during the June season) in order to minimize the insolation effect. For example, the SZA range at the magnetic north pole, as specified at http://www.ngdc.noaa.gov/geomag/GeomagneticPoles.shtml,
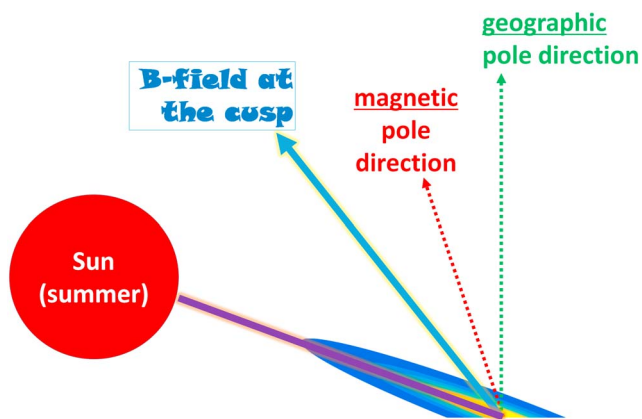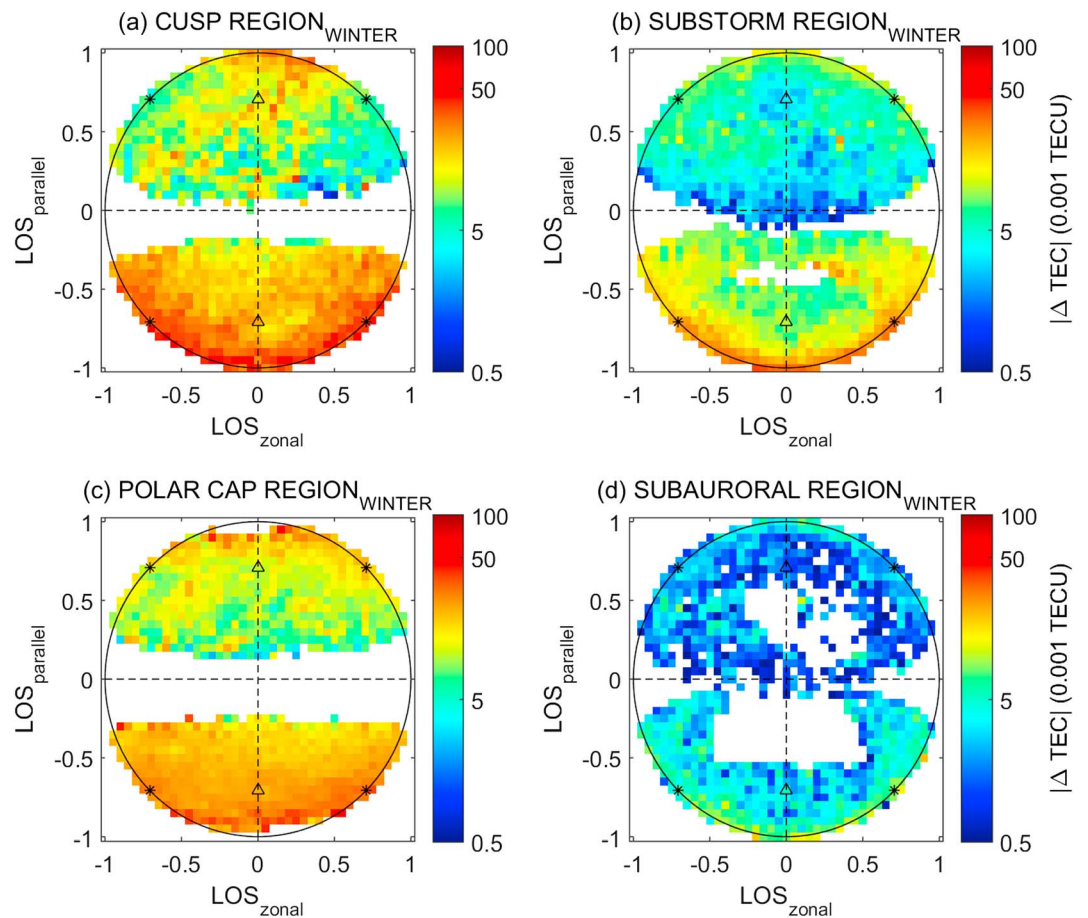

Figure 14. Schematic illustration of ionospheric perturbation orientation under combined magnetic field and insolation effect for the SH around the December solstice (local summer).

**Figure 15.** The same as Figure 9, but only with the Swarm-Alpha data points from local winter conditions.

for the June (December) solstice is 62°–70° (109°–117°). Similarly, the SZA range at the magnetic south pole for the June (December) solstice day is 87°–139° (40°–92°). This clearly shows the much larger SZA range in the SH.

In each panel of Figures 15 and 16, the |ΔTEC| in the SH (i.e., points above the abscissa) is now better aligned with the unit circle in comparison to those in Figures 9 and 10. If we focus on the SH data (i.e., above the abscissa), high |ΔTEC| values located off the unit circle in Figures 9 and 10 have largely disappeared in Figures 15 and 16. Now the |ΔTEC| in the SH is generally higher near the unit circle than far from the circle. General trends in Swarm-Bravo data are similar to those of Swarm-Alpha. Figures 15 and 16 further support our suggestion that the SH |ΔTEC| values in Figures 9 and 10 are not well aligned with the unit circle (or the local L shell) because a significant part of LEO-VTEC gradients are generated by insolation effects.

4.3. Different Degrees of Cross-L Elongation in Different Subregions

In Section 3, we argued that |ΔTEC| decreases with increasing LOS deviation from the plane tangent to the local L shell, but at different rates for different subregions (i.e., cusp, substorm, polar cap, and subauroral regions). In this subsection, we will test the argument more quantitatively. Figure 17 demonstrates how |ΔTEC| decreases with increasing LOS deviation from the direction tangent to the local L shell, as presented by $\rho = \sqrt{y^2 + z^2} = \sqrt{LOS_{zonal}^2 + LOS_{parallel}^2}$ (see Figure 3). When ρ is 1 or 0, the LOS direction is tangent or normal to the local L shell, respectively. Different colors are used for the different subregions, which are detailed in the legend. Big symbols connected with lines represent |ΔTEC| averages for a given range of ρ. Note that the |ΔTEC| values within a given subregion are normalized by the same constant. The purpose of the normalization is to force the big symbols for different subregions to pass the (1, 1) point in Figure 17. In that way, we can quantitatively intercompare the decrease rates of |ΔTEC| with respect to ρ at the different subregions. Note that underpopulated bins (number of data points per bin <50,000) are not shown in Figure 17. The good bin population (≥50,000) in all the four subregions supports the reliability of the results in Figure 17.
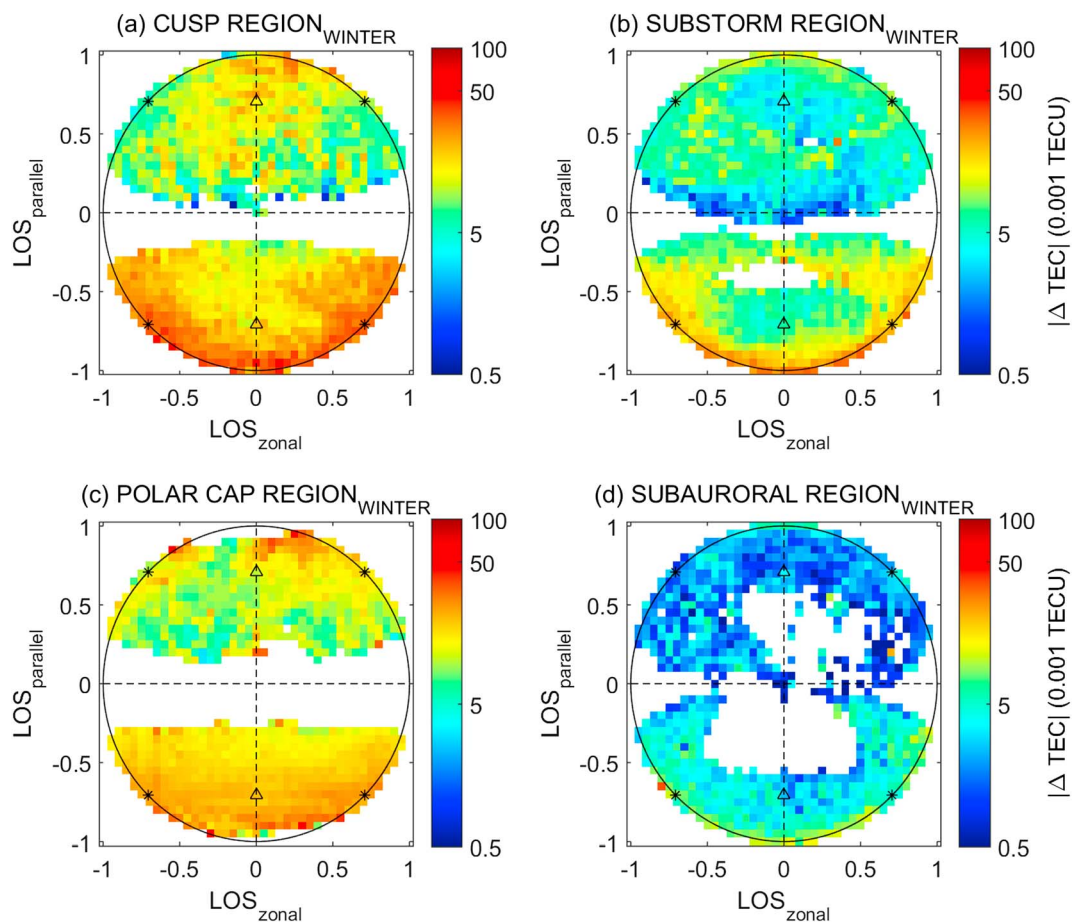
Figure 16. The same as Figure 15, but for Swarm-Bravo.

The standard error of the mean (standard deviation divided by the square root of the bin population) is also shown as error bars, but the values are so small that they are almost indistinguishable from the symbols. Figure 17a is for Swarm-Alpha and Figure 17b for Swarm-Bravo. Only data from the NH under local winter conditions are used. However, even if we repeat the data processing with local winter data points from both hemispheres, the results remain qualitatively the same.

In Figure 17a, |ΔTEC| decreases as the LOS approaches the L shell normal direction (i.e., from right to left along the abscissa). However, the decrease is much faster in the substorm and subauroral regions than in the polar cap region. We may conclude that plasma perturbations in the polar cap region are not only aligned with the local L shell but also elongated significantly in the direction normal to the L shell (e.g., in the noon-midnight directions). The results of Swarm-Bravo (Figure 17b) are generally consistent with the Swarm-Alpha data.

The cross-L morphology of polar cap perturbations may suggest that polar cap patches (PCPs) and the tongue of ionization (TOI), both of which characterize the TEC perturbations in the polar cap, are significantly elongated across different L shells. This result qualitatively agrees with previous studies. For example, equatorward moving PCPs in *Hosokawa et al.* [2016a, Figure 2] can be considered to be elongated perpendicular to the motion [so-called cigar shapes, e.g., *Hosokawa et al.*, 2016b] but contain fingerlike (scale size ∼55–210 km) substructures pointing toward the wake. The fingers are considered to originate from gradient drift instability. As the PCPs in *Hosokawa et al.* [2016a, Figure 2] approximately move antisunward and equatorward (i.e., across different L shells), they can be considered to have overall structures elongated tangent to L shells and to contain substructures (fingers) pointing in cross-L directions; the combined morphology is compatible with our results in Figure 17. Also, *Förster and Haaland* [2015] concluded that the high-latitude convection is dominated by the two-cell pattern for most of the interplanetary magnetic field directions. Resultant antisunward convection in the middle of the polar cap can lead to (segmented or unsegmented) TOI [e.g., *Zhang et al.*, 2013; *Walsh et al.*, 2014], which is elongated across different L shells by definition. Note that TOIs can occur
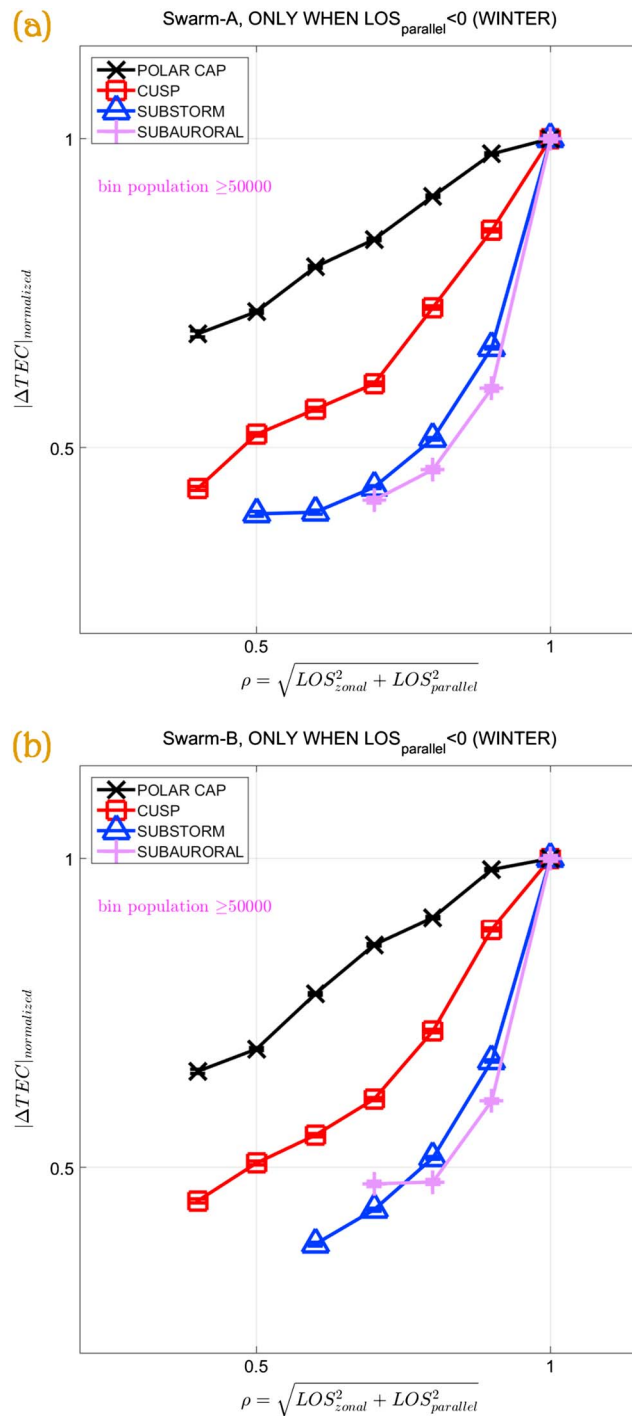
Figure 17. Dependence of |ΔTEC| on the LOS deviation from the direction tangent to the local L shell under the NH local winter conditions: (a) for Swarm-Alpha and (b) for Swarm-Bravo. The abscissa corresponds to ρ in Figure 3. When ρ is 1 and 0, the LOS direction is tangent and normal to the local L shell, respectively.

during strong as well as moderate to weak geomagnetic storms [e.g., *Liu et al.*, 2015, and references therein]. As our study imposes no constraints on geomagnetic activity, TOIs will also contribute to the statistics in the polar cap, as shown in Figures 9 and 10.

As for substorm regions, on the other extreme, we expect zonally elongated perturbations [e.g., *Moen et al.*, 2015, Figure 8] caused by the zonally diverging convection pattern near the nightside reconnection region. This can explain the Swarm/TEC observations of the largest |ΔTEC| on the unit circle (Figures 15b and 16b).

Similarly, reasonably good alignment of the midlatitude (subauroral) troughs with the L shell, which can be deduced from the MLT-L diagrams of the trough minima [*Lee et al.*, 2011, Figure 2], can contribute to the similar behavior of the subauroral perturbations to that in the substorm regions. Note that high-latitude plasma convection patterns mentioned above for the subauroral region are also important for forming the midlatitude troughs [*Lee et al.*, 2011, and references therein]. Intermediate behavior of the cusp perturbations can be partly attributed to particle precipitations in the cusp [e.g., *Goodwin et al.*, 2015], which can add fine structures to the perturbations convected from the dayside midlatitude regions.

In summary, differences in perturbation shape in the various subregions at high latitudes can largely be attributed to plasma convection direction (e.g., gradient drift instability in the polar cap) and particle precipitation morphology (e.g., further structuring in the cusp). The convection goes across the L shell direction in a large part of the polar cap, while in the nightside substorm region (and just poleward of the subauroral region) convection is more aligned with the L shell.

4.4. Geolocation Approach

TEC observations derived from ground-based GNSS receivers are frequently "geolocated" with respect to a piercing point at an assumed ionospheric altitude, e.g., the *F* region peak height [e.g., *Nishioka et al.*, 2009]. In case of LEO-TEC observations, some studies also used this geolocation approach by assuming a thin ionosphere a certain distance above the LEO satellite [e.g., *Zakharenkova et al.*, 2016], while others directly assign the observed TEC value to the LEO satellite position [e.g., *Mannucci et al.*, 2005]. Both approaches are simple approximations because the actual ionospheric density is varying continuously with height. In this study, we have applied the latter approach, assigning LEO-VTEC perturbations to the Swarm locations. The rationale for that is the Swarm orbit altitude (above 450 km), which is generally above the *F* region peak height [e.g., *Burns et al.*, 2012]. This means plasma density typically decreases above Swarm altitude, and the largest contributions to TEC gradients come from locations close to the satellite.

It is difficult to pinpoint the true altitude of LEO-VTEC perturbations. In order to justify the assignment of recorded TEC perturbations to the satellite position, we have imposed another constraint: significant fluctuations of in situ plasma density at the Swarm position have to be observed simultaneously; see section 2.3. In that case, we expect that local perturbations make dominant contributions to the LEO-VTEC results. Only these are considered in our analysis in the LOS space, such as in Figures 9 and 10. This line of arguments is visualized in Figure 11, illustrating that the dependence of |ΔTEC| on LOS directions can be used for interpreting the morphology of plasma density perturbations.

5. Summary and Conclusion

In this study, we have analyzed TEC data along the LOS between Swarm and GNSS satellites during the period from 16 July 2014 to 15 July 2016. From the data set, we have investigated the dependence of the LEO-VTEC gradient (|ΔTEC|) on the relationship between LOS directions and background geomagnetic field. Note that the |ΔTEC| is calculated from differences among three consecutive data points along the Swarm satellite track (i.e., 7.5 km/s × 2 ≈ 15 km). The horizontal scale size is within the perturbation scale sizes producing GNSS radio occultation scintillation (1–40 km) [e.g., *Shume et al.*, 2015]. Keeping this caveat in mind, our observational results can be summarized as follows:

1. The climatological distribution of |ΔTEC| in geographic and geomagnetic coordinate systems is in general agreement with previous results of CHAMP-VTEC observations presented by *Noja et al.* [2013].
2. The |ΔTEC| values of Swarm-Alpha (near 470 km altitude) are generally larger by <20% than those of Swarm-Bravo (near 520 km altitude), as expected from the longer ray path through the ionosphere for the former. The altitude dependence is weaker in the SH during the June solstice.
3. In the NH, |ΔTEC| is higher when the LOS is better aligned with the local L shell surface. The sensitivity to L shell alignment is highest (lowest) for the substorm/subauroral (polar cap) region.
4. In the SH, large |ΔTEC| values can be observed even for LOS directions that deviate clearly from the plane tangent to the local L shell. The SH results agree better with the NH results if only data points under local winter conditions with weaker insolation effects are considered.

From these observational results, we can deduce the morphology (equivalently, anisotropy or preferred direction of elongation) of the high-latitude LEO-VTEC perturbations as follows:

1. In the NH, the high-latitude LEO-VTEC perturbations do not only occur aligned with the B field but can also be found tangent to the L shell surface.
2. In the NH, the LEO-VTEC perturbations in the polar cap (in the substorm/subauroral region) exhibit more (less) elongation normal to the L shell than in the other high-latitude subregions.
3. In the SH, the $|\Delta TEC|$ structures exhibit significant misalignment from the local L shells and are offset toward the Sun. The large offset between geographic and geomagnetic poles in the SH, and as a consequence the large variation of the solar illumination angle, can lead to various orientations of $|\Delta TEC|$ structures.

As the expected lifetime of the Swarm constellation is about 10 years, we can revisit the issue near the end of the mission. The larger data set in future will enable us to investigate whether the conclusions of this study are valid throughout the solar cycle.

References

Aikio, A. T., K. Mursula, S. Buchert, F. Forme, O. Amm, G. Marklund, M. Dunlop, D. Fontaine, A. Vaivads, and A. Fazakerley (2004), Temporal evolution of two auroral arcs as measured by the cluster satellite and coordinated ground-based instruments, *Ann. Geophys.*, 22, 4089–4101.

Burns, A. G., S. C. Solomon, W. Wang, L. Qian, Y. Zhang, and L. J. Paxton (2012), Daytime climatology of ionospheric NmF2 and hmF2 from COSMIC data, *J. Geophys. Res.*, 117, A09315, doi:10.1029/2012JA017529.

Clausen, L. B. N., J. I. Moen, K. Hosokawa, and J. M. Holmes (2016), GPS scintillations in the high latitudes during periods of dayside and nightside reconnection, *J. Geophys. Res. Space Physics*, 121(4), 3293–3309, doi:10.1002/2015JA022199.

Förster, M., and S. Haaland (2015), Interhemispheric differences in ionospheric convection: Cluster EDI observations revisited, *J. Geophys. Res. Space Science*, 120, 5805–5823, doi:10.1002/2014JA020774.

Forte, B., and S. M. Radicella (2004), Geometrical control of scintillation indices: What happens for GPS satellites, *Radio Sci.*, 39, RS5014, doi:10.1029/2002RS002852.

Forte, B., C. Coleman, S. Skone, I. Hggström, C. N. Mitchell, J. Kinrade, and G. S. Bust (2016), Identification of scintillation signatures on GPS signals originating from plasma structures detected with EISCAT incoherent scatter radar along the same line of sight, *J. Geophys. Res. Space Physics*, 121, doi:10.1002/2016JA023271.

Garcia-Fernàndez, M., and O. Montenbruck (2006), Low Earth orbit satellite navigation errors and vertical total electron content in single-frequency GPS tracking, *Radio Sci.*, 41, RS5001, doi:10.1029/2005RS003420.

Goodwin, L. V., et al. (2015), Swarm in situ observations of F region polar cap patches created by cusp precipitation, *Geophys. Res. Lett.*, 42, 996–1003, doi:10.1002/2014GL062610.

Heise, S., N. Jakowski, A. Wehrenpfennig, C. H. Reigber, and H. Lühr (2002), Sounding of the topside ionosphere/plasmasphere based on GPS measurements from CHAMP: Initial results, *Geophys. Res. Lett.*, 29(14), 1699, doi:10.1029/2002GL014738.

Hosokawa, K., S. Taguchi, and Y. Ogawa (2016a), Edge of polar cap patches, *J. Geophys. Res. Space Physics*, 121, 3410–3420, doi:10.1002/2015JA021960.

Hosokawa, K., S. Taguchi, and Y. Ogawa (2016b), Periodic creation of polar cap patches from auroral transients in the cusp, *J. Geophys. Res. Space Physics*, 121(6), 5639–5652, doi:10.1002/2015JA022221.

Kil, H. (2015), The morphology of equatorial plasma bubbles — A review, *J. Astron. Space Sci.*, 32(1), 13–19, doi:10.5140/JASS.2015.32.1.13.

Kinrade, J., C. N. Mitchell, P. Yin, N. Smith, M. J. Jarvis, D. J. Maxfield, M. C. Rose, G. S. Bust, and A. T. Weatherwax (2012), Ionospheric scintillation over Antarctica during the storm of 5–6 April 2010, *J. Geophys. Res.*, 117, A05304, doi:10.1029/2011JA017073.

Lear, W. M. (1987), *GPS Navigation for Low-Earth Orbiting Vehicles*, NASA 87-FM-2, JSC-32031, rev. 1, Lyndon B, Johnson Space Cent., Houston, Tex.

Lee, I. T., W. Wang, J. Y. Liu, C. Y. Chen, and C. H. Lin (2011), The ionospheric midlatitude trough observed by FORMOSAT-3/COSMIC during solar minimum, *J. Geophys. Res.*, 116, A06311, doi:10.1029/2010JA015544.

Lee, H.-B., G. Jee, Y. H. Kim, and J. S. Shim (2013), Characteristics of global plasmaspheric TEC in comparison with the ionosphere simultaneously observed by Jason-1 satellite, *J. Geophys. Res. Space Physics*, 118, 935–946, doi:10.1002/jgra.50130.

Lei, J., Q. Zhu, W. Wang, A. G. Burns, B. Zhao, X. Luan, J. Zhong, and X. Dou (2015), Response of the topside and bottomside ionosphere at low and middle latitudes to the October 2003 superstorms, *J. Geophys. Res. Space Physics*, 120, 6974–6986, doi:10.1002/2015JA021310.

Liu, J., T. Nakamura, L. Liu, W. Wang, N. Balan, T. Nishiyama, M. R. Hairston, and E. G. Thomas (2015), Formation of polar ionospheric tongue of ionization during minor geomagnetic disturbed conditions, *J. Geophys. Res. Space Physics*, 120, 6860–6873, doi:10.1002/2015JA021393.

Lühr, H., J. Park, J. W. Gjerloev, J. Rauberg, I. Michaelis, J. M. G. Merayo, and P. Brauer (2015), Field-aligned currents' scale analysis performed with the Swarm constellation, *Geophys. Res. Lett.*, 42, 1–8, doi:10.1002/2014GL062453.

Mannucci, A. J., B. T. Tsurutani, B. A. Iijima, A. Komjathy, A. Saito, W. D. Gonzalez, F. L. Guarnieri, J. U. Kozyra, and R. Skoug (2005), Dayside global ionospheric response to the major interplanetary events of October 29–30, 2003 Halloween storms, *Geophys. Res. Lett.*, 32, L12S02, doi:10.1029/2004GL021467.

Mitchell, C. N., L. Alfonsi, G. De Franceschi, M. Lester, V. Romano, and A. W. Wernik (2005), GPS TEC and scintillation measurements from the polar ionosphere during the October 2003 storm, *Geophys. Res. Lett.*, 32, L12S03, doi:10.1029/2004GL021644.

Moen, J., K. Hosokawa, N. Gulbrandsen, and L. B. N. Clausen (2015), On the symmetry of ionospheric polar cap patch exits around magnetic midnight, *J. Geophys. Res. Space Physics*, 120, 7785–7797, doi:10.1002/2014JA020914.

Muella, M. T. A. H., E. A. Kherani, E. R. de Paula, A. P. Cerruti, P. M. Kintner, I. J. Kantor, C. N. Mitchell, I. S. Batista, and M. A. Abdu (2010), Scintillation-producing Fresnel-scale irregularities associated with the regions of steepest TEC gradients adjacent to the equatorial ionization anomaly, *J. Geophys. Res.*, 115, A03301, doi:10.1029/2009JA014788.

Nishioka, M., A. Saito, and T. Tsugawa (2009), Super-medium-scale traveling ionospheric disturbance observed at midlatitude during the geomagnetic storm on 10 November 2004, *J. Geophys. Res.*, 114, A07310, doi:10.1029/2008JA013581.

Noja, M. (2010), Retrieval of plasmaspheric total electron content from space-based GPS observations including a receiver differential code bias and multipath estimation, Master Thesis, Hochschule Neubrandenburg.

Noja, M., C. Stolle, J. Park, and H. Lühr (2013), Long-term analysis of ionospheric polar patches based on CHAMP TEC data, *Radio Sci.*, 48, 289–301, doi:10.1002/rds.20033.

Olsen, N., et al. (2013), The swarm satellite constellation application and research facility (SCARF), *Earth Planets Space*, 65, 1189–1200.

Park, J., R. Ehrlich, H. Lühr, and P. Ritter (2012), Plasma perturbations in the high-latitude ionospheric F-region and their diamagnetic signatures as observed by CHAMP, *J. Geophys. Res.*, *117*, A10322, doi:10.1029/2012JA018166.

Park, J., H. Lühr, and M. Noja (2015), Three-dimensional morphology of equatorial plasma bubbles deduced from measurements onboard CHAMP, *Ann. Geophys.*, *33*, 129–135, doi:10.5194/angeo-33-129-2015.

Pedatella, N. M., and K. M. Larson (2010), Routine determination of the plasmapause based on COSMIC GPS total electron content observations of the midlatitude trough, *J. Geophys. Res.*, *115*, A09301, doi:10.1029/2010JA015265.

Pedatella, N. M., J. M. Forbes, A. Maute, A. D. Richmond, T.-W. Fang, K. M. Larson, and G. Millward (2011), Longitudinal variations in the F region ionosphere and the topside ionosphere-plasmasphere: Observations and model simulations, *J. Geophys. Res.*, *116*, A12309, doi:10.1029/2011JA016600.

Prikryl, P., P. T. Jayachandran, S. C. Mushini, and R. Chadwick (2011), Climatology of GPS phase scintillation and HF radar backscatter for the high-latitude ionosphere under solar minimum conditions, *Ann. Geophys.*, *29*, 377–392, doi:10.5194/angeo-29-377-2011.

Richmond, A. D. (1995), Ionospheric electrodynamics using magnetic apex coordinates, *J. Geomag. Geoelectr.*, *47*(2), 191–212.

Shume, E. B., A. Komjathy, R. B. Langley, O. Verkhoglyadova, M. D. Butala, and A. J. Mannucci (2015), Intermediate-scale plasma perturbations in the polar ionosphere inferred from GPS radio occultation, *Geophys. Res. Lett.*, *42*, 688–696, doi:10.1002/2014GL062558.

Stolle, C., R. Floberghagen, H. Lühr, S Maus, D. Knudsen, P. Alken, E. Doornbos, B. Hamilton, A. Thomson, and P. Visser (2013), Space weather opportunities from the Swarm mission including near real time applications, *Earth Planets Space*, *65*(111), 1375–1383, doi:10.5047/eps.2013.10.002.

IJssel, v. d., B. F. Jose, and O. Montenbruck (2016), Impact of Swarm GPS receiver updates on POD performance, *Earth Planets Space*, *68*, 85.

Walsh, B. M., J. C. Foster, P. J. Erickson, and D. G. Sibeck (2014), Simultaneous ground- and space-based observations of the plasmaspheric plume and reconnection, *Science*, *343*(6175), 1122–1125, doi:10.1126/science.1247212.

Xiong, C., C. Stolle, and H. Lühr (2016), The Swarm satellite loss of GPS signal and its relation to ionospheric plasma perturbations, *Space Weather*, *14*, 563–577, doi:10.1002/2016SW001439.

Yizengaw, E., M. B. Moldwin, A. Komjathy, and A. J. Mannucci (2006), Unusual topside ionospheric density response to the November 2003 superstorm, *J. Geophys. Res.*, *111*, A02308, doi:10.1029/2005JA011433.

Yue, X., W. S. Schreiner, D. C. Hunt, C. Rocken, and Y.-H. Kuo (2011), Quantitative evaluation of the low Earth orbit satellite based slant total electron content determination, *Space Weather*, *9*, S09001, doi:10.1029/2011SW000687.

Zakharenkova, I., and E. Astafyeva (2015), Topside ionospheric perturbations as seen from multisatellite observations, *J. Geophys. Res. Space Physics*, *120*, 807–824, doi:10.1002/2014JA020330.

Zakharenkova, I., E. Astafyeva, and I. Cherniak (2016), GPS and in situ Swarm observations of the equatorial plasma density irregularities in the topside ionosphere, *Earth Planets Space*, *2016*(68), 120, doi:10.1186/s40623-016-0490-5.

Zhang, Q.-H., et al. (2013), Direct observations of the evolution of polar cap ionization patches, *Science*, *339*(6127), 1597–1600, doi:10.1126/science.1231487.